Organic-Acid-Assisted Fabrication of Low-Cost Li-Rich Cathode Material (Li[Li$_{1/6}$Fe$_{1/6}$Ni$_{1/6}$Mn$_{1/2}$]O$_2$) for Lithium−Ion Battery

Taolin Zhao,[†] Shi Chen,[†] Li Li,*,[†] Xiaoxiao Zhang,[†] Huiming Wu,[‡] Tianpin Wu,[§] Cheng-Jun Sun,[§] Renjie Chen,[†] Feng Wu,[†] Jun Lu,*,[‡] and Khalil Amine*,[‡]

[†]School of Chemical Engineering and the Environment, Beijing Key Laboratory of Environmental Science and Engineering, Beijing Institute of Technology, Beijing 100081, People's Republic of China

[‡]Chemical Sciences and Engineering Division, Argonne National Laboratory, Lemont, Illinois 60439, United States

[§]X-ray Science Division, Argonne National Laboratory, Lemont, Illinois 60439, United States

ABSTRACT: A novel Li-rich cathode Li[Li$_{1/6}$Fe$_{1/6}$Ni$_{1/6}$Mn$_{1/2}$]O$_2$ (0.4Li$_2$MnO$_3$—0.6LiFe$_{1/3}$Ni$_{1/3}$Mn$_{1/3}$O$_2$) was synthesized by a sol−gel method, which uses citric acid (SC), tartaric acid (ST), or adipic acid (SA) as a chelating agent. The structural, morphological, and electrochemical properties of the prepared samples were characterized by various methods. X-ray diffraction showed that single-phase materials are formed mainly with typical α-NaFeO$_2$ layered structure (R$\bar{3}$m), and the SC sample has the lowest Li/Ni cation disorder. The morphological study indicated homogeneous primary particles in good distribution size (100 nm) with small aggregates. The Fe, Ni, and Mn valences were determined by X-ray absorption near-edge structure analysis. In coin cell tests, the initial reversible discharge capacity of an SA electrode was 289.7 mAh g^{-1} at the 0.1C rate in the 1.5−4.8 V voltage range, while an SC electrode showed a better cycling stability with relatively high capacity retention. At the 2C rate, the SC electrode can deliver a discharge capacity of 150 mAh g^{-1} after 50 cycles. Differential capacity vs voltage curves were employed to further investigate the electrochemical reactions and the structural change process during cycling. This low-cost, Fe-based compound prepared by the sol−gel method has the potential to be used as the high capacity cathode material for Li−ion batteries.

KEYWORDS: Fe-based, sol−gel method, lithium-rich, cathode material, lithium−ion battery, low-cost
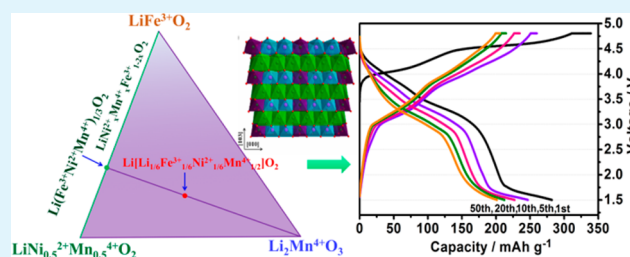
1. INTRODUCTION

For some time now, Li−ion batteries have been used as electrochemical power sources in consumer electronics and are now being considered for electric vehicle (EV) applications. The most commonly used cathode material since Li−ion batteries were commercialized by Sony in 1991,[1] LiCoO$_2$, has toxicity, cost, and safety issues. For the past decade, alternative cathode materials, such as LiNi$_{1/3}$Mn$_{1/3}$Co$_{1/3}$O$_2$, LiMn$_2$O$_4$, and LiFePO$_4$, have been extensively examined.[2−4] While the cycling stability and rate capabilities of these materials have been significantly improved, their reversible lithium storage capacity is limited by the low theoretical capacity. These cathode materials cannot meet the energy density and power density demands for the extended driving range of EVs. Exploration of alternative cathode materials with high capacity and low cost is, therefore, essential for developing the next generation of high-energy and high-power Li−ion batteries.

Developed by Thackeray et al.,[5,6] the layered-structure cathodes composites of LiMO$_2$ (R$\bar{3}$m) and Li$_2$MnO$_3$ (C2/m) (also called "Li-rich" or "Mn-rich" cathodes) can be expressed as xLi$_2$MO$_3$·(1−x)LiMO$_2$ (M = Ni, Co, Mn, Fe, Cr, or combination) or standard chemical formula as Li$_{1+x}$M$_{1−x}$O$_2$. The relationship of layered LiMO$_2$ and Li$_2$MnO$_3$ can be described conveniently by the tetrahedral diagram, as shown in Figure 1a. Two enlarged phase diagrams (Figure 1b,c) have been drawn in order to describe the Li-rich layered oxide. Because of the high capacity and high output voltage of these Li-rich, Mn-rich layered materials, researchers around the world have invested great effort in investigating them as cathodes for Li−ion batteries.[7] Compared to traditional cathode materials such as LiCoO$_2$ and LiMn$_2$O$_4$, the typical compositions of these cathodes, Li[Li$_{0.2}$Ni$_{0.2}$M$_{0.6}$]O$_2$[8,9] and Li[Li$_{0.2}$Ni$_{0.13}$Co$_{0.13}$Mn$_{0.54}$]O$_2$,[10,11] can deliver much higher capacity (>250 mAh g^{-1}) after activation of the Li$_2$MnO$_3$ component in the initial charge. However, a low-cost Li-rich cathode is still needed for the EV application.

Iron has been used to prepare cobalt-free Li-rich cathode materials due to its low cost and non-toxicity. For example, Tabuchi et al. recently developed a LiFeO$_2$—Li$_2$MnO$_3$ solid solution as new high-capacity cathode material.[12−18] This material has shown a capacity of >220 mAh g^{-1}, and the redox of Fe^{3+}/Fe^{4+} (4.0−4.5 V) has been detected by ^{57}Fe Mössbauer
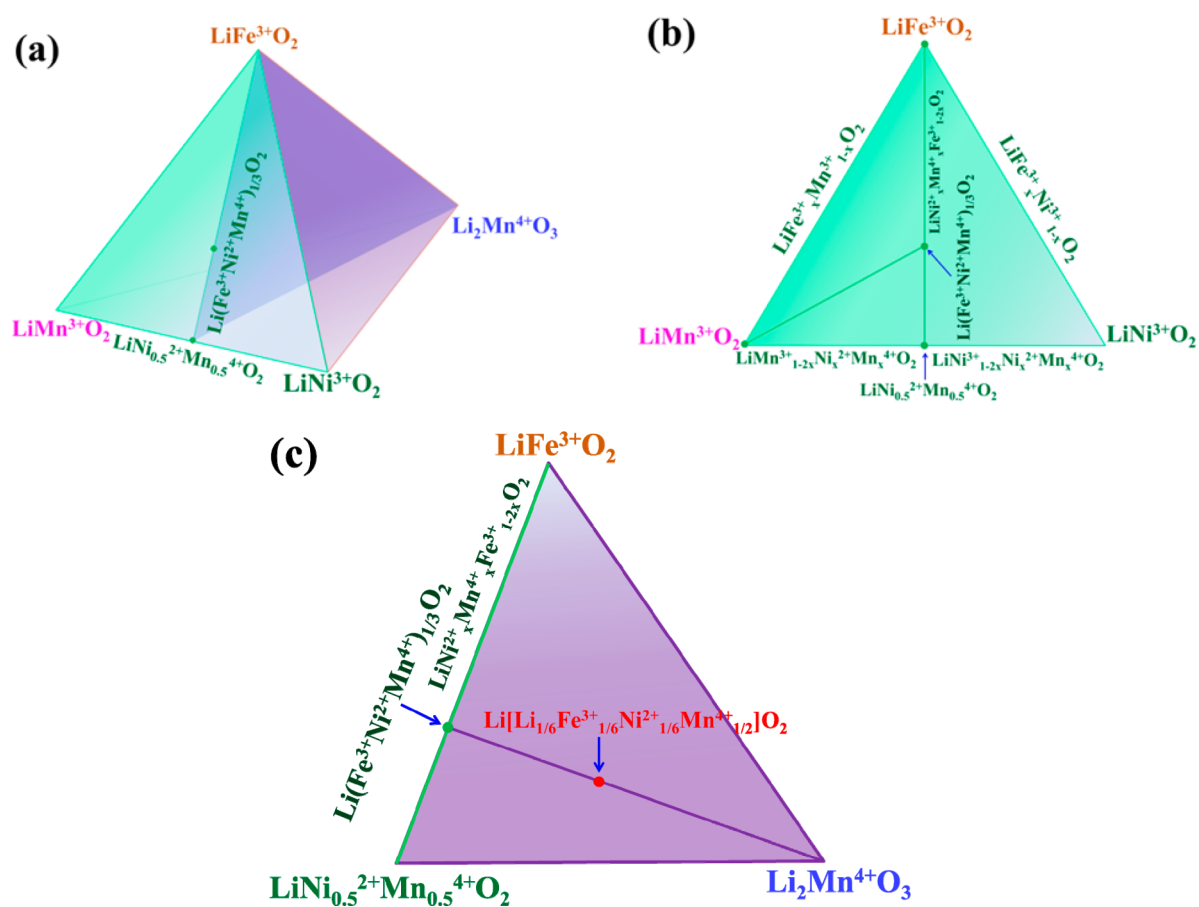
Figure 1. Compositional phase diagram of (a) layered lithium transition metal oxide: $LiFeO_2$—$LiNiO_2$—$LiMnO_2$—Li_2MnO_3; (b) lithium—stoichiometric layered transition metal oxide: $LiFeO_2$—$LiNiO_2$—$LiMnO_2$; and (c) lithium-rich Mn-based layered oxide: $LiFeO_2$—$LiNi_{0.5}Mn_{0.5}O_2$—Li_2MnO_3.
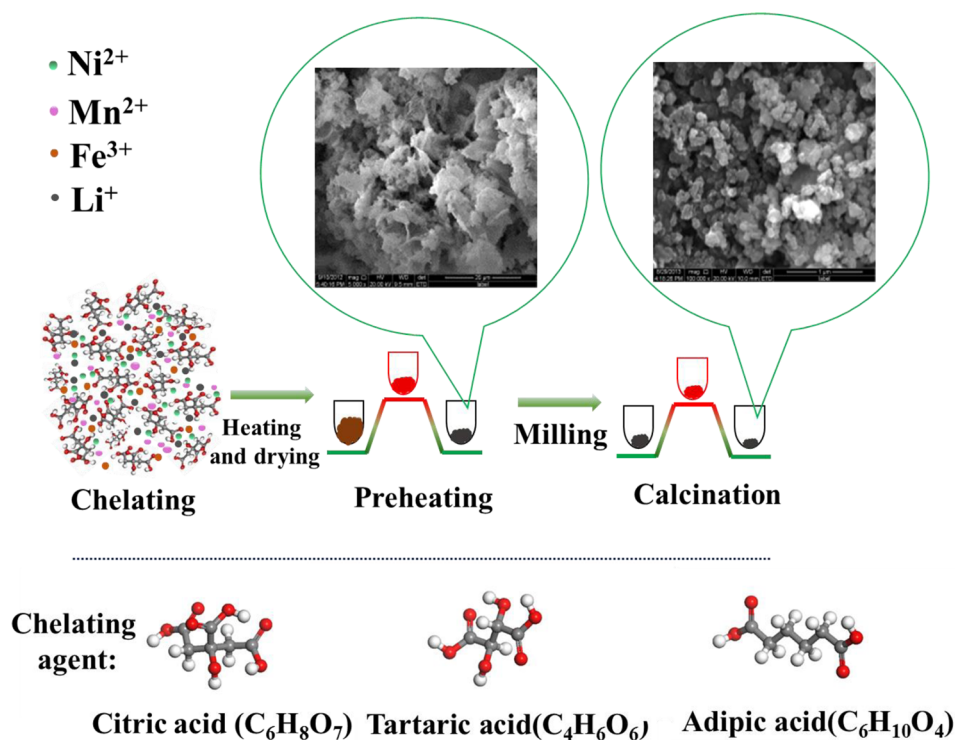

Figure 2. Synthesis flow diagram of $Li[Li_{1/6}Fe_{1/6}Ni_{1/6}Mn_{1/2}]O_2$ samples prepared with different chelating agents.
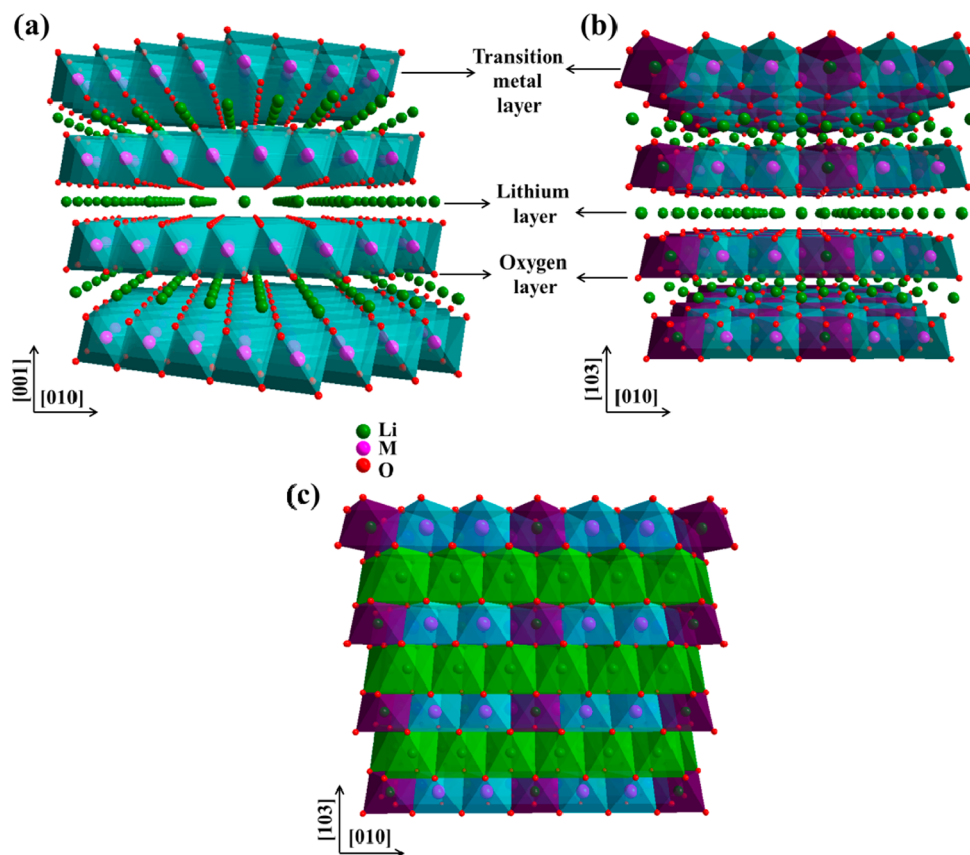
Figure 3. (a) Crystal structure of the layered rhombohedral oxide $LiMO_2$ structure (space group: $R\bar{3}m$, M = Ni, Co, Mn, Fe, Cr, etc.). (b) Crystal structure of the monoclinic Li_2MnO_3 structure (space group: $C2/m$) viewed from the [100] crystallographic direction. In the Li_2MnO_3 structure, lithium ions occupy transition metal layer as well as lithium layer. (c) Homogeneous Li-rich solid solution structure with partial ordered $C2/m$ monoclinic phase viewed from the [100] crystallographic direction.

spectra during the first charge/discharge. It has been reported that the substitution of Mn in Li_2MnO_3 by other 3d transition metals (e.g., Fe and Ni) in these Li-rich composites offers lower cost and higher potential with higher energy density than those of existing active materials.[19−21] The cycling stability and Coulombic efficiency of these composites could be also improved through simple doping or substitution by other transition metals like Ti.[17] Although many researchers have focused on developing these materials, the capacity retention, cycling stability, and rate capability still need to be improved. A path to such improvement is development of a new method or composition that will yield a cathode with improved structure, high electrochemical performance, and low cost.

We have applied the sol−gel method to synthesize a low−cost cathode material with a composition of $Li[Li_{1/6}Fe_{1/6}Ni_{1/6}Mn_{1/2}]O_2$ ($0.4Li_2MnO_3−0.6LiFe_{1/3}Ni_{1/3}Mn_{1/3}O_2$), as shown in Figure 1. Various analyses of this composite material were conducted to examine the crystal structure, morphology, and transition metal valence state. We also investigated the effect of different chelating agents (citric acid, tartaric acid, and adipic acid) on the structure and electrochemical performance of Li-$[Li_{1/6}Fe_{1/6}Ni_{1/6}Mn_{1/2}]O_2$.

2. EXPERIMENTAL SECTION

2.1. Synthesis. In this work, all the chemicals were of analytical grade and were used as-received without further purification. The cathode material $Li[Li_{1/6}Fe_{1/6}Ni_{1/6}Mn_{1/2}]O_2$ was prepared by the sol−gel method, involving the use of chelating agents (citric acid, tartaric acid, or adipic acid). Stoichiometric amounts of $Li(CH_3COO)\cdot2H_2O$,
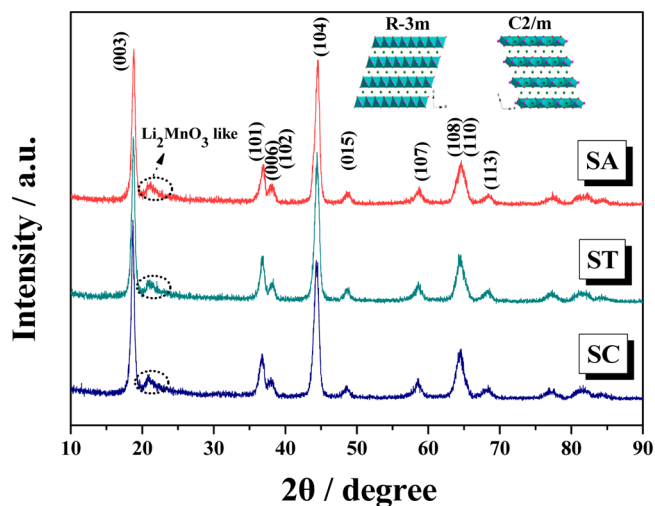

Figure 4. XRD patterns of $Li[Li_{1/6}Fe_{1/6}Ni_{1/6}Mn_{1/2}]O_2$ samples prepared with different chelating agents.

$Fe(NO_3)_3\cdot9H_2O$, $Ni(CH_3COO)_2\cdot4H_2O$, and $Mn(CH_3COO)_2\cdot4H_2O$ were dissolved in deionized water to obtain a transparent solution, which was introduced dropwise to a beaker with the acid solution. In this process, the pH value of the mixed solution was adjusted to 7 by adding aqueous ammonia. Then, the resulting solution was heated at 80 °C with vigorous stirring to remove the water slowly until a transparent sol and then gel were obtained. After drying, the gel was preheated at 400 °C for 4 h in air to eliminate organic components. Then, the obtained bulk powder was ground uniformly and calcined

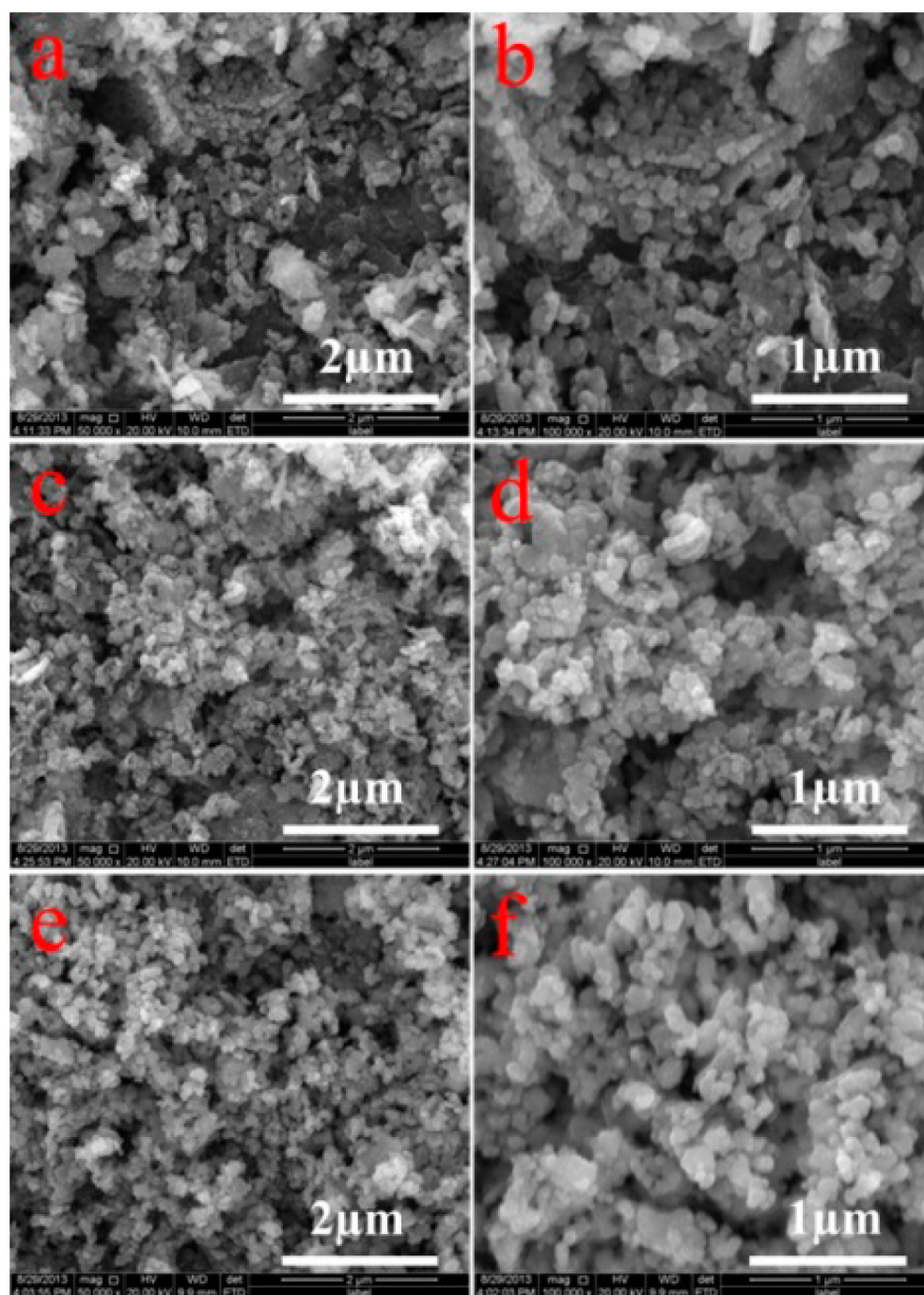**Figure 5.** Scanning electron micrographs of Li[Li$_{1/6}$Fe$_{1/6}$Ni$_{1/6}$Mn$_{1/2}$]O$_2$ samples at magnifications of ×50k and ×100k: (a and b) SC, (c and d) ST, and (e and f) SA.

at 700 °C in air for 16 h to obtain well−formed powder Li[Li$_{1/6}$Fe$_{1/6}$Ni$_{1/6}$Mn$_{1/2}$]O$_2$. The flowchart and the structures of chelating agents are shown in Figure 2. The samples prepared with the different chelating agents are denoted as SC (citric acid), ST (tartaric acid), and SA (adipic acid).

2.2. Material Characterization. A structural analysis was carried out using X-ray diffraction (XRD, Rigaku Ultima IV−185) with a Cu Kα radiation source. The source voltage and current were 40 kV and 40 mA, respectively. Data were acquired with a step size of 8° min^{-1} over a 2θ range of 10°−90°. The morphologies of the prepared samples were characterized by field-emission scanning electron microscopy (FE-SEM, Quanata 200f). Element mapping and chemical composition of the prepared samples were determined with an energy dispersive X-ray detector (EDX). The valence state of the Fe, Mn, and

Ni ions was determined by K-edge X-ray absorption ear edge spectroscopy (XANES), which were performed at Sector 20 at the Advanced Photon Source using beamline 20-BM with the focused beam size of ~400 × 400 μm^2 in fwhm, the energy resolution is about $\Delta E/E = 1.3 \times 10^{-4}$ by using a Si (111) monochromator. A Rh-coated harmonic rejection mirror and a 15% detuning of the beam intensity were applied to reject the higher energy harmonics. The Fe, Mn, and Ni metal foil samples were also used as an online reference for the measurements.

2.3. Electrochemical Tests. For fabrication of the cathodes, the prepared powders were mixed with acetylene black and polyvinylidene fluoride (8:1:1 by weight) in N-methyl-2-pyrrolidone (NMP). The obtained slurry was coated onto Al foil and roll-pressed. The electrodes were dried overnight at 80 °C in a vacuum oven before use.

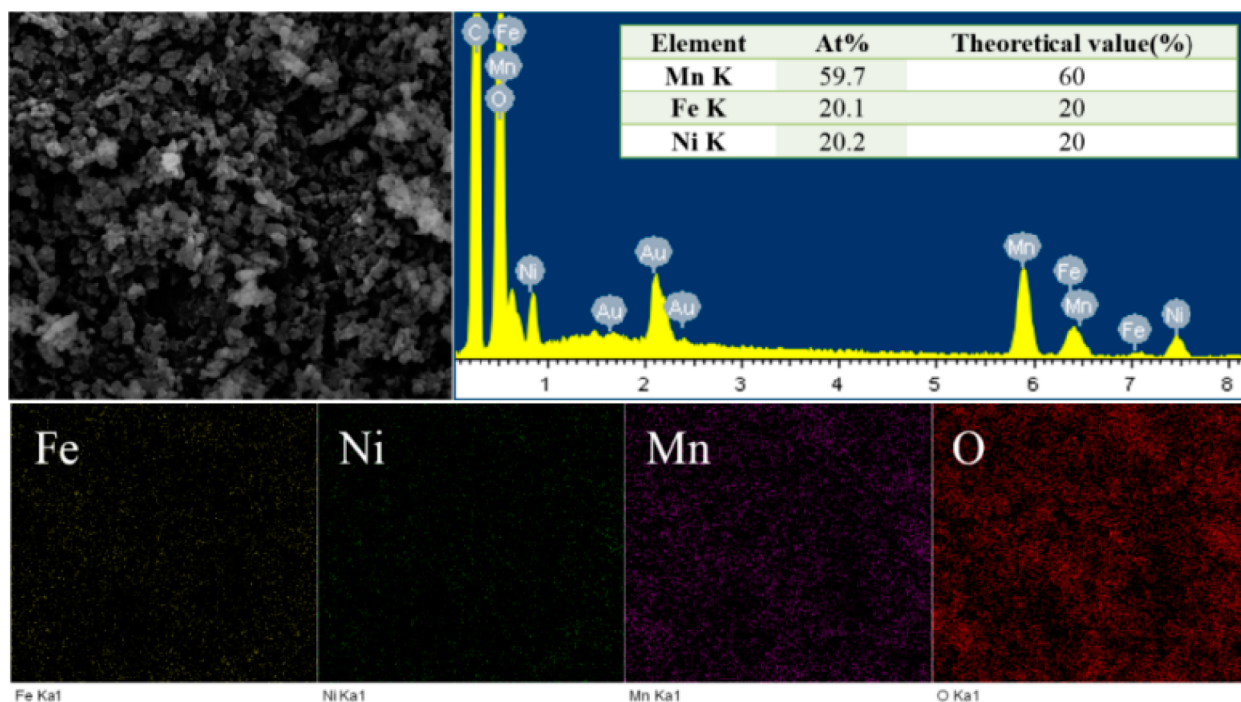| Element	At%	Theoretical value(%)
Mn K	59.7	60
Fe K	20.1	20
Ni K	20.2	20

Figure 6. EDX image and element distributions of SC sample.

The anode was lithium metal. The electrode materials were assembled into 2025 button cells in a glovebox filled with high−purity argon. The electrolyte solution was 1 M $LiPF_6$ in ethyl carbonate and dimethyl carbonate in a 1:1 ratio (by volume). Charge/discharge tests were performed with a Land battery test system (Land CT2001A, Wuhan, China) in the voltage range of 2.0−4.8 V and 1.5−4.8 V at different current rates with current densities from 20 mA g^{-1} (0.1C) to 400 mA g^{-1} (2C). A two−step charge process was employed: constant-current charge followed by an additional constant-voltage charge until the current density dropped to half of its initial value.

3. RESULTS AND DISCUSSION

3.1. XRD Structural Analysis. Because of the importance of the relationship between the electrode microstructure and electrochemical performance, it is essential to determine the crystal structure of this Li-rich cathode to understand and precisely improve its electrochemical performance. The crystal structures of rhombohedral $LiMO_2$ (space group: $R\bar{3}m$, M = Co, Ni, Mn, Fe, Cr, etc.) and monoclinic Li_2MnO_3 (space group: $C2/m$) viewed from their [100] crystallographic direction are shown in Figure 3(a),(b). Both of these structures can be considered as layered α-$NaFeO_2$-type rock salt, and all the octahedral sites are occupied by close-packed oxygen arrays. For the $LiMO_2$ structure, the transition metal layers are occupied by only transition metal ions, whereas for the Li_2MnO_3 structure, the Li^+ and Mn^{4+} ions occupy the transition metal layer. In general, the structure of the lithium-rich cathode can arise from layered $LiMO_2$ with α-$NaFeO_2$ rock salt, with excess lithium ions occupying the transition metal layer, as shown in Figure 3(c). The octahedral sites of the cubic close−packed oxygen arrays are all occupied. Figure 4 shows the XRD patterns obtained for the three $Li[Li_{1/6}Fe_{1/6}Ni_{1/6}Mn_{1/2}]O_2$ samples. Except for the low-intensity peaks around 20−23°, the other diffraction peaks are indexed based on the typical hexagonal α-$NaFeO_2$ layered structure with $R\bar{3}m$ space group, indicating the formation of a pure phase structure without any impurities. In addition, the two weak superlattice peaks

at $2\theta = 20-23°$ are considered to be caused by the short-range ordering of Li, Ni, Mn, and Fe in the 3a sites, indicating an integrated monoclinic Li_2MnO_3 phase ($C2/m$ symmetry).[22]

In the XRD reflections of all three samples, the crystallinity is lower than other Li-rich cathode without Fe due to the lower calcination temperature. A typical layered material is indicated by the $I_{(003)}/I_{(104)}$ intensity ratio and clear splitting of the (006)/(102) and the (108)/(110) peaks. The ratios of $I_{(003)}/I_{(104)}$ are 1.2834, 1.0957, and 1.0752 for SC, ST, and SA, respectively, indicating that the SC sample shows the lowest degree of cation disordering between the Li (3a) and the transition metal sites (3b) of the hexagonal layered structure.[23] This finding suggests that good electrochemical performance can be expected.

3.2. SEM and EDX Analysis. The morphologies of the $Li[Li_{1/6}Fe_{1/6}Ni_{1/6}Mn_{1/2}]O_2$ samples were investigated by SEM (Figure 5). Disperse primary particles with sharp edges and uniform size and distribution (100−200 nm) can be observed for all three samples. It is well-known that the morphology and size distribution of the particles are of great importance to Li−ion battery performance. Generally, lithium insertion/extraction is much easier with active materials having small particle size due to the reduction of Li^+ diffusion. As a result, faster electronic transport can be realized with small particles,[24−26] significantly improving rate performance. Among the three samples, the SC sample exhibits a slightly smaller particle size with a more uniform size distribution, which is essential for better rate performance. In addition, the interconnected network of the particles resulting from small agglomeration could enhance the electrode−electrolyte interfacial area by providing a path for better Li^+ diffusion. Overall, the $Li[Li_{1/6}Fe_{1/6}Ni_{1/6}Mn_{1/2}]O_2$ composites synthesized by the sol−gel method have a morphological structure beneficial to good electrochemical performance.

The composition of the prepared samples was further examined by EDX, taking SC as a representative example
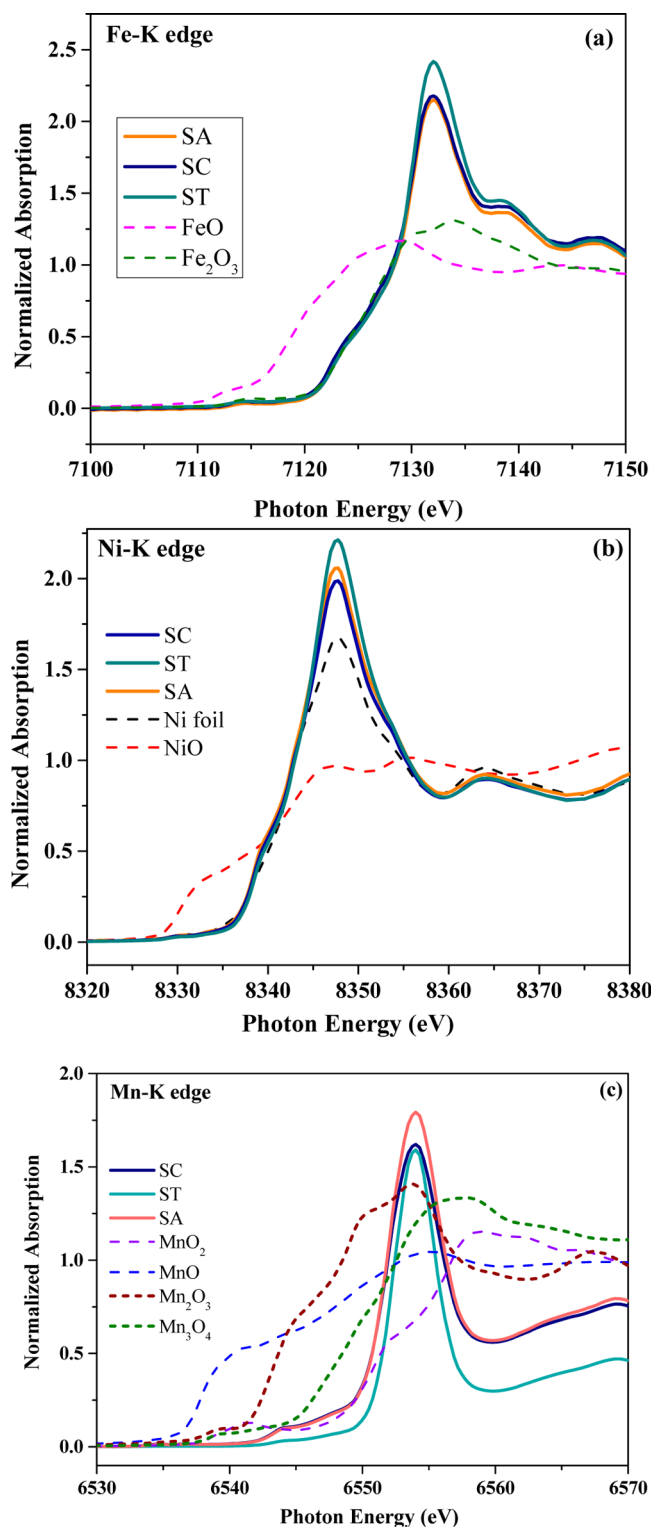
Figure 7. K-edge XANES patterns of (a) Fe; (b) Ni, and (c)Mn for Li[Li$_{1/6}$Fe$_{1/6}$Ni$_{1/6}$Mn$_{1/2}$]O$_2$ samples.

(Figure 6). The elements Fe, Mn, Ni, and O are homogeneously distributed in the sample, as shown at the bottom of Figure 6. The inserted table to Figure 6 (upper right) lists the calculated compositions of Fe, Mn, and Ni in the SC sample. The measured molar ratios of the Fe, Ni, and Mn are approximately the same as the theoretical values of 1:1:3, indicating that the sample was synthesized with good stoichiometry.
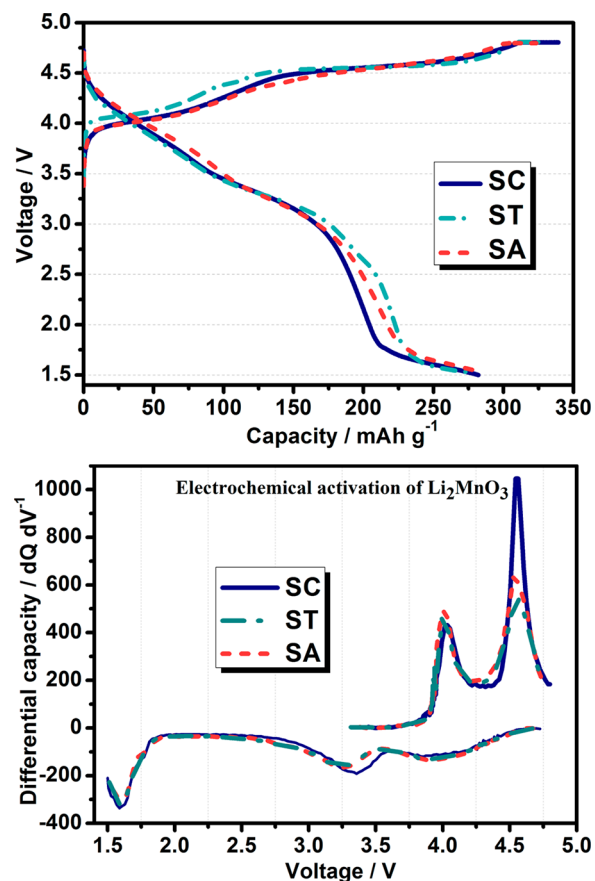

Figure 8. Initial charge/discharge curves at 0.1C rate of Li-[Li$_{1/6}$Fe$_{1/6}$Ni$_{1/6}$Mn$_{1/2}$]O$_2$ electrodes.
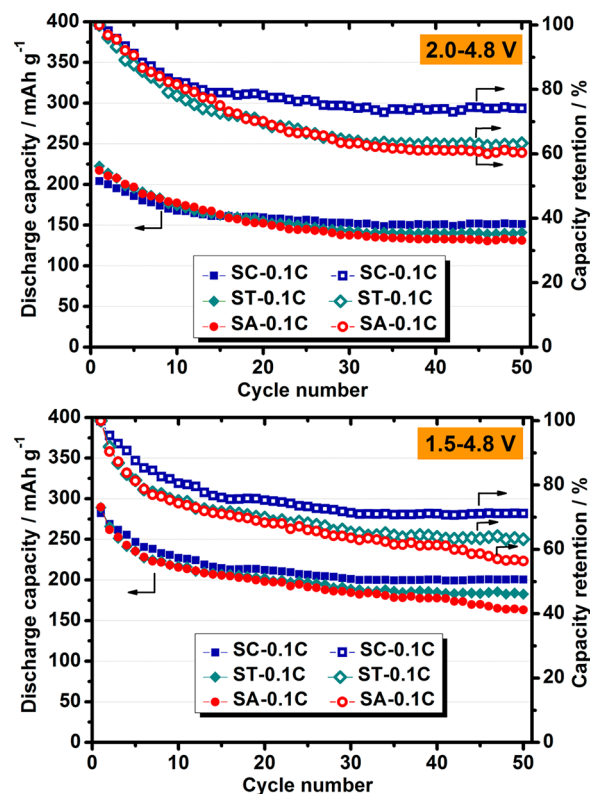
Figure 9. Cycling performance of Li[Li$_{1/6}$Fe$_{1/6}$Ni$_{1/6}$Mn$_{1/2}$]O$_2$ electrodes in different voltage ranges at 0.1 C rate.

Table 1. Initial Charge and Discharge Capacities, Coulombic Efficiencies, And Irreversible Capacity Losses at 0.1C Rate of Li[Li$_{1/6}$Fe$_{1/6}$Ni$_{1/6}$Mn$_{1/2}$]O$_2$ Electrodes

samples	first charge capacity (mAh g^{-1})	first discharge capacity (mAh g^{-1})		initial coulombic efficiency (%)		irreversible capacity loss (mAh g^{-1})	
		2−4.8 V	1.5−4.8 V	2−4.8 V	1.5−4.8 V	2−4.8 V	1.5−4.8 V
SC	339.2	204.2	282	60.2	83.1	135.0	57.2
ST	326.6	222.6	289.1	68.2	88.5	104	37.5
SA	327.2	217.3	289.7	66.4	88.5	109.9	37.5
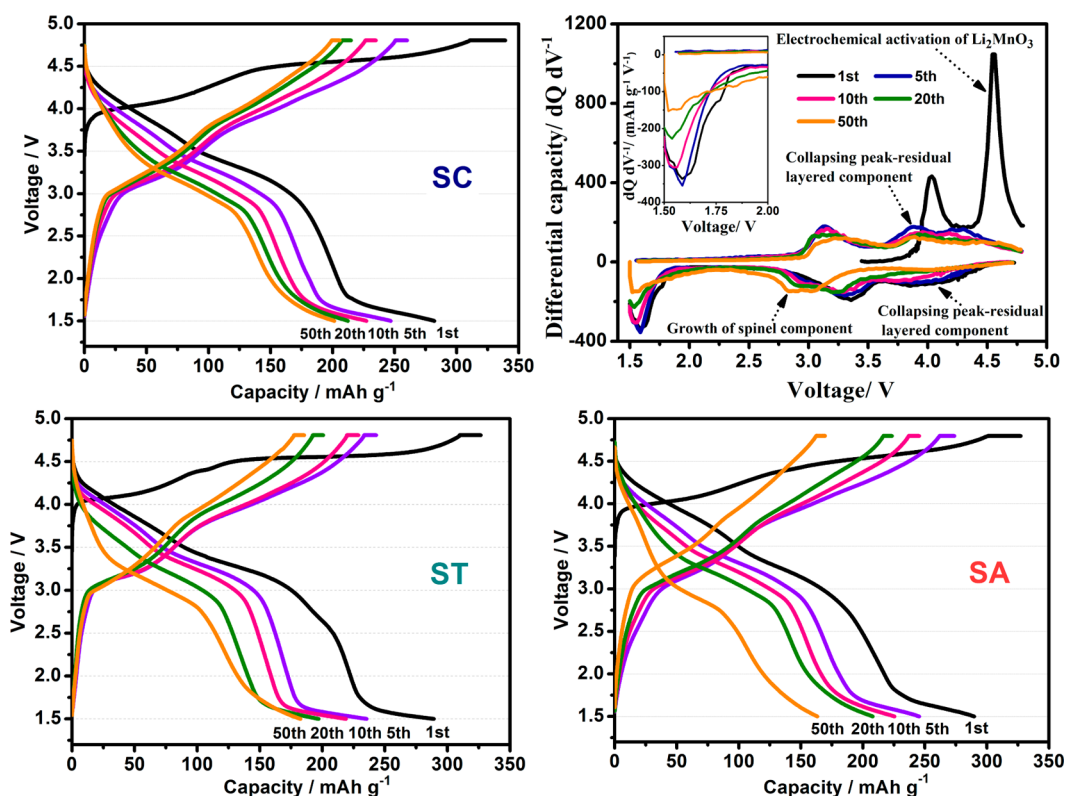
Figure 10. Charge/discharge profiles at 0.1C rate of 1st, 5th, 10th, 20th, and 50th cycles for Li[Li$_{1/6}$Fe$_{1/6}$Ni$_{1/6}$Mn$_{1/2}$]O$_2$ electrodes and the differential capacity vs voltage curves of the SC electrode.

3.3. XANES Analysis. The chemical compositions of the prepared samples were also determined using XANES spectra recorded in air at room temperature. To facilitate these measurements, XANES reference spectra were recorded for standard chemicals, for instance Fe foil, FeO, and Fe$_2$O$_3$ standards for Fe K-edge, as shown in in Figure 7. Edge position of XANES is typically used to determine the oxidation states of the elements in the compounds. On the basis of the XANES results shown in Figure 7, it is obvious that the oxidation state of Fe in the sample is close to Fe (III).[27] The Mn K-edge XANES spectra showed that the oxidation state of Mn for all samples is 4+, while the Ni K-edge XANES spectra showed that the oxidation state of Ni for all samples is 2+.

3.4. Initial Charge/Discharge Performance. Galvanostatic charge/discharge studies were performed in tests with the half-cell configuration at different current densities and ambient temperature. Figure 8 shows the initial charge/discharge curves and the corresponding differential capacity versus voltage (dQ/dV) plots in the voltage range of 1.5−4.8 V at the 0.1C rate. The curves are similar for all the electrodes, which also achieved excellent capacity. During charging, the curves show turning point at 4.5 V, indicating lithium extraction from LiMO$_2$- and Li$_2$MnO$_3$-like components, and verifying that this type of

Li-rich electrode material consists of two components.[28] The voltage plateaus below 4.5 V which comes from the lithium extraction from lithium ion layer in LiMO$_2$ component, represent the formal oxidation processes of Ni^{2+} to Ni^{4+} and Fe^{3+} to Fe^{4+}. The occurrence of electrochemical reactions of Fe ion is a characterization of Li-rich cathode containing Fe. An irreversible voltage plateau results from an irreversible reaction above 4.5 V, that is, the lithium extraction and oxygen release (Li$_2$O) from the Li$_2$MnO$_3$ lattice, followed by activation of the oxidation states of Mn.[29] During discharging, all the samples show the same trend with discharge plateaus at 4.0 V, 3.3 V, and below 2.0 V. The 4.0 V plateau reflect the reductions of Ni^{4+} and Fe^{4+}. The reduction to Mn^{3+} of Mn^{4+}, activated by the release of oxygen, is indicated by the reduction peak at 3.3 V. The irreversible peak observed below 2.0 V may be related to the electrochemical reaction of Fe^{3+} to Fe^{2+},[30,31] which is different from Li-rich cathodes without Fe.

The initial charge and discharge capacities, Coulombic efficiencies, and irreversible capacity loss of all three electrodes at various voltage ranges are listed in Table 1. The SC electrode has the highest initial charge capacity (339.2 mAh g^{-1}), while the SA electrode exhibits a higher initial discharge capacity of 289.7 mAh g^{-1} compared with that of SC electrode (282 mAh g^{-1}).
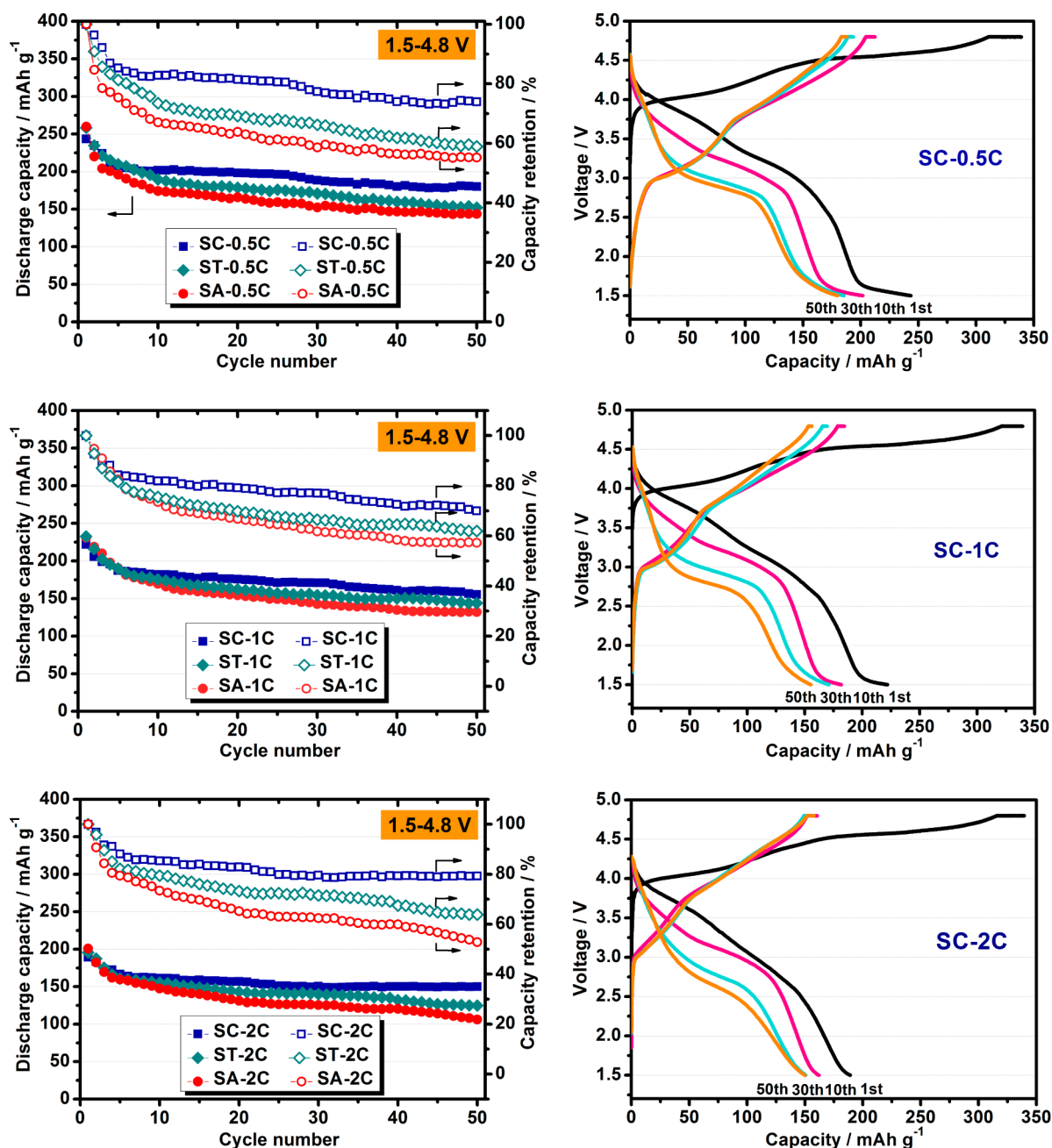
Figure 11. Cycling performance and charge/discharge voltage curves at different cycles and rates (0.5, 1, and 2C) of $Li[Li_{1/6}Fe_{1/6}Ni_{1/6}Mn_{1/2}]O_2$ electrodes over 1.5−4.8 V range.

The initial Coulombic efficiencies of the electrodes discharged to 1.5 and 2.0 V are roughly 80−90% and 60−70%, respectively.

3.5. Cycling Performance. Figure 9 shows the cycling stability and capacity retention of the SC, ST, and SA electrodes cycled at 0.1C over different voltage ranges (1.5−4.8 V and 2.0−4.8 V). The same trends are observed for the cycling performance of all three electrodes at the two voltage ranges over 50 cycles. For the 1.5−4.8 V voltage range, the discharge capacity gradually decreases to different degrees during the initial ten cycles. Although the SA electrode has the highest initial discharge capacity among the three tested electrodes, its capacity retention is the lowest after 50 cycles (56.4%). Meanwhile, the capacity fade rate of the SC electrode is lower than the other two electrodes, and the capacity retention is 71.1% after 50 cycles. In general, the retained

discharge capacities after 50 cycles in the 1.5−4.8 V test follow the trend: SC (200.5 mAh g^{-1}) > ST (182.6 mAh g^{-1}) > SA (163.3 mAh g^{-1}). Compared with the other two electrodes, the SC electrode shows better cycling stability with relatively high capacity retention in the 1.5−4.8 V test. Similarly, when cycled between 2 and 4.8 V, the SC electrode attained the highest discharge capacity after 50 cycles, 151.2 mAh g^{-1}, with the highest capacity retention (74.1%).

To further investigate the capacity fading mechanism, we obtained charge/discharge curves of the three electrodes at several different cycles in the voltage range of 1.5−4.8 V. The results are shown in Figure 10 and Table 2. The discharge capacity of all the materials degrades mainly in the initial 10 cycles and remains stable in the following 40 cycles. The SC electrode showed the best capacity retention over the 50 cycles

Table 2. Discharge Capacities (mAh g^{-1}) and Capacity Retentions at Various Rates and Voltage Ranges for Li[Li$_{1/6}$Fe$_{1/6}$Ni$_{1/6}$Mn$_{1/2}$]O$_2$ Electrodes

	cycle number	0.1C (2−4.8 V)	0.1C (1.5−4.8 V)	0.5C (1.5−4.8 V)	1C (1.5−4.8 V)	2C (1.5−4.8 V)
SC	1st	204.2	282	243.3	221.9	189.1
	5th	185.9	246.9	207.6	187.1	166.7
	10th	167.8	227.2	201.7	181.7	161.4
	20th	159.5	212.3	198.2	175.7	156.8
	50th	151.2	200.5	180	155.3	150
	capacity retention (50th)	74.0%	71.1%	74.0%	70.0%	79.3%
ST	1st	222.6	289.1	258.2	232.6	195.5
	5th	195.2	235.5	209.9	189.8	160.7
	10th	173.9	217	189.7	175.6	155.4
	20th	155.1	202.1	178.5	162.4	143.2
	50th	140.9	182.6	152.2	144	124.8
	capacity retention (50th)	63.3%	63.2%	58.9%	61.9%	63.8%
SA	1st	217.3	289.7	259.9	230.9	200.9
	5th	196.9	235.4	195.9	190.5	159.5
	10th	177.3	215.5	174.3	169.7	147.6
	20th	152.3	198	165.9	154.2	131.1
	50th	131.1	163.3	143.6	132.1	106.2
	capacity retention (50th)	60.3%	56.4%	55.3%	57.2%	52.9%

(70−80%). The discharge capacities for this electrode at the 0.1C rate are 282, 246.9, 227.2, 212.3, and 200.5 mAh g^{-1} for the first, fifth, 10th, 20th, and 50th cycles, respectively. In addition, the midpoint voltages also are lower with increasing numbers of cycles, and the SC electrode shows the lowest rate of voltage degradation.

Differential capacity vs voltage plots of the SC electrode at the same cycle intervals and the 0.1C rate are also shown in Figure 10. After the initial electrochemical activation of the Li$_2$MnO$_3$ component above 4.5 V, a dominant reversible redox reaction occurs around 3 V and becomes apparent as the redox reaction peaks (3.4 V/3.9 V) of the layered structure weaken gradually.[32] This finding indicates that the layered structure of the SC sample is gradually transformed to a spinel component, and an unexpected layered−spinel intergrowth structure is formed on cycling. The inset to Figure 10 shows the differential capacity vs voltage plots of the SC electrode in the voltage range of 1.5−2 V. It can be seen that the reduction peak of Fe ion diminishes during cycling.

The reason for capacity fading is critical to understand the as-prepared cathode material. Compared with some other Li-rich cathodes without Fe element, the crystal structure of our prepared low-cost Li-rich cathode material containing Fe is not so good because of the lower calcination temperature. In addition, the reduction peak of Fe ion diminishing with cycling is also considered to be related with the capacity fading.

3.6. Rate Performance. The three electrodes (SC, ST, and SA) were also cycled in the 1.5−4.8 V range at various rates (0.5C, 1C, and 2C), and the results are given in Figure 11 and Table 2. As the applied current density increases, only the surfaces of the active materials participate in the reaction,[19] meaning a reduction of the time for Li$^+$ intercalation into the crystal lattice. Consequently, the discharge capacities for all three electrodes decrease gradually due to their increasing polarization at high current density. Although the SC electrode delivers the lowest discharge capacity at the first cycle among the three electrodes, it shows a relatively moderate capacity fade and delivers the highest discharge capacity at each current density from 0.1C to 2C after 50 cycles, as shown in Figure 12. The discharge capacities and capacity retentions of the SC
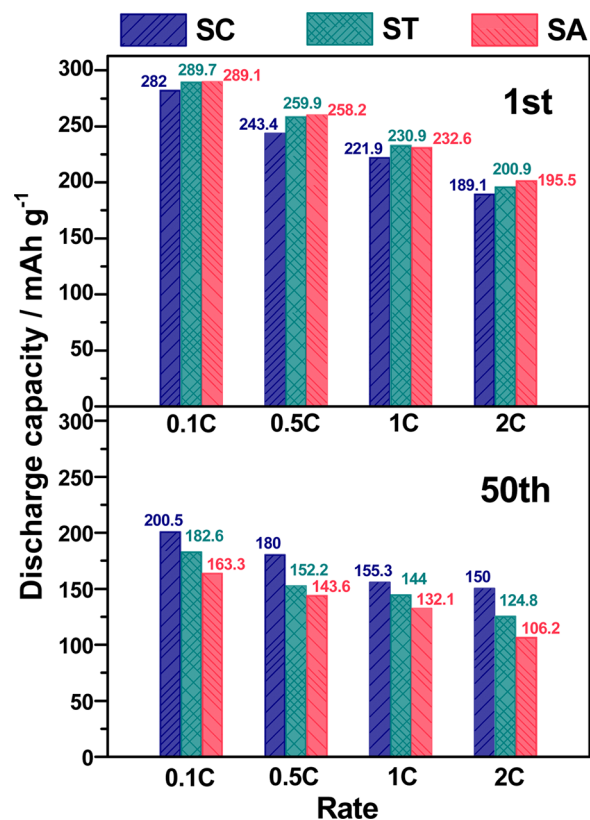

Figure 12. Discharge capacities at different rates (0.1, 0.5, 1, and 2C) between first and 50th cycles with Li[Li$_{1/6}$Fe$_{1/6}$Ni$_{1/6}$Mn$_{1/2}$]O$_2$ electrodes.

electrodes are the highest for the tested rates. The charge/discharge voltage curves of the SC electrode at different rates are also shown in Figure 11. Its discharge capacity at the 2C rate is 150 mAh g^{-1} after 50 cycles, about 79.3% of the discharge capacity obtained at the first cycle (189.1 mAh g^{-1}). In general, the rate capability decreases in the following order: SC, ST, then SA.

4. CONCLUSIOSN

Low-cost, Li-rich cathode materials with the composition $Li[Li_{1/6}Fe_{1/6}Ni_{1/6}Mn_{1/2}]O_2$ were prepared by a facile sol−gel method with different chelating agents (citric acid, tartaric acid, and adipic acid). The synthesized materials exhibited remarkable cycling performance and rate capability. The initial discharge capacity of the SC electrode exceeded 282 mAh g^{-1} at the 0.1C rate, and the capacity retention approached 71.1% after 50 cycles. When cycled at 2C, about 150 mA h g^{-1} discharge capacity was obtained after 50 cycles. Morphological and structural analysis, along with the electrochemical cell tests of the materials, revealed that the high discharge capacity and rate performance could be attributed to the Li-rich layered structure, the interconnected nanoparticles, and the redox reactions of $Ni^{2+/4+}$ and $Fe^{3+/4+}$. As Li-rich Fe-based layered structure, the low-cost $Li[Li_{1/6}Fe_{1/6}Ni_{1/6}Mn_{1/2}]O_2$ composite may be a promising cathode with high capacity and eco-friendliness for Li−ion batteries, although the electrochemical performance could be further improved by simple coating or doping. Taking the convenient and accessible sol−gel preparation method into consideration, we propose that it is an effective synthesis route for future commercialization of low-cost cathodes for Li−ion batteries with good performance.

■ AUTHOR INFORMATION

Corresponding Authors
*E-mail: lily863@bit.edu.cn.
*E-mail: junlu@anl.gov.
*E-mail: amine@anl.gov.

Notes
The authors declare no competing financial interest.

■ ACKNOWLEDGMENTS

■ REFERENCES

(1) Koksbang, R.; Barker, J.; Shi, H.; Saidi, M. Y. Cathode Materials for Lithium Rocking Chair Batteries. *Solid State Ionics* **1996**, *84*, 1−21.
(2) Ohzuku, T.; Kitagawa, M.; Hirai, T. Electrochemistry of Manganese Dioxide in Lithium Nonaqueous Cell. III-X-Ray Diffrac-tional Study on the Reduction of Spinel-Related Manganese Dioxide. *J. Electrochem. Soc.* **1990**, *137*, 769−775.
(3) Ohzuku, T.; Makimura, Y. Layered Lithium Insertion Material of $LiCo_{1/3}Ni_{1/3}Mn_{1/3}O_2$ for Lithium-Ion Batteries. *Chem. Lett.* **2001**, *7*, 642−643.
(4) Padhi, A. K.; Nanjundaswamy, K. S.; Goodenough, J. B. Phospho-Olivines as Positive-Electrode Materials for Rechargeable Lithium Batteries. *J. Electrochem. Soc.* **1997**, *144*, 1188−1194.
(5) Thackeray, M. M.; Johnson, C. S.; Vaughey, J. T.; Li, N.; Hackney, S. A. Advances in Manganese-Oxide 'Composite' Electrodes for Lithium-Ion Batteries. *J. Mater. Chem.* **2005**, *15*, 2257−2267.
(6) Thackeray, M. M.; Kang, S.-H.; Johnson, C. S.; Vaughey, J. T.; Benedek, R.; Hackney, S. A. Li_2MnO_3-Stabilized $LiMO_2$ (M = Mn, Ni, Co) Electrodes for Lithium-Ion Batteries. *J. Mater. Chem.* **2007**, *17*, 3112−3125.
(7) Yu, H.; Zhou, H. High-Energy Cathode Materials (Li_2MnO_3−$LiMO_2$) for Lithium−Ion Batteries. *J. Phys. Chem. Lett.* **2013**, *4*, 1268−1280.
(8) Wang, D.; Belharouak, I.; Zhou, G.; Amine, K. Nanoarchitecture Multi-Structural Cathode Materials for High Capacity Lithium Batteries. *Adv. Funct. Mater.* **2013**, *23*, 1070−1075.
(9) Zheng, J.; Gu, M.; Xiao, J.; Zuo, P.; Wang, C.; Zhang, J.-G. Corrosion/Fragmentation of Layered Composite Cathode and Related Capacity/Voltage Fading During Cycling Process. *Nano Lett.* **2013**, *13*, 3824−3830.
(10) Zhao, T.; Li, L.; Chen, S.; Chen, R.; Zhang, X.; Lu, J.; Wu, F.; Amine, K. The Effect of Chromium Substitution on Improving Electrochemical Performance of Low-Cost Fe−Mn Based Li-Rich Layered Oxide as Cathode Material for Lithium-Ion Batteries. *J. Power Sources* **2014**, *245*, 898−907.
(11) Zhang, X.; Belharouak, I.; Li, L.; Lei, Y.; Elam, J. W.; Nie, A.; Chen, X.; Yassar, R. S.; Axelbaum, R. L. Structural and Electrochemical Study of Al_2O_3 and TiO_2 Coated $Li_{1.2}Ni_{0.13}Mn_{0.54}Co_{0.13}O_2$ Cathode Material Using ALD. *Adv. Energy. Mater.* **2013**, *3*, 1299−1307.
(12) Tabuchi, M.; Nakashima, A.; Shigemura, H.; Ado, K.; Kobayashi, H.; Sakaebe, H.; Kageyama, H.; Nakamura, T.; Kohzaki, M.; Hirano, A.; Kanno, R. Synthesis, Cation Distribution, and Electrochemical Properties of Fe-Substituted Li_2MnO_3 as a Novel 4V Positive Electrode Material. *J. Electrochem. Soc.* **2002**, *149*, A509−A524.
(13) Tabuchi, M.; Shigemura, H.; Ado, K.; Kobayashi, H.; Sakaebe, H.; Kageyama, H.; Kanno, R. Preparation of Lithium Manganese Oxides Containing Iron. *J. Power Sources* **2001**, *97−98*, 415−419.
(14) Tabuchi, M.; Nabeshima, Y.; Ado, K.; Shikano, M.; Kageyama, H.; Tatsumi, K. Material Design Concept for Fe-Substituted Li_2MnO_3-Based Positive Electrodes. *J. Power Sources* **2007**, *174*, 554−559.
(15) Tabuchi, M.; Nabeshima, Y.; Takeuchi, T.; Tatsumi, K.; Imaizumi, J.; Nitta, Y. Fe Content Effects on Electrochemical Properties of Fe-Substituted Li_2MnO_3 Positive Electrode Material. *J. Power Sources* **2010**, *195*, 834−844.
(16) Tabuchi, M.; Nabeshima, Y.; Takeuchi, T.; Kageyama, H.; Tatsumi, K.; Akimoto, J.; Shibuya, H.; Imaizumi, J. Synthesis and Electrochemical Characterization of Fe and Ni Substituted Li_2MnO_3—An Effective Means to Use Fe for Constructing "Co-Free" Li_2MnO_3 Based Positive Electrode Material. *J. Power Sources* **2011**, *196*, 3611−3622.
(17) Tabuchi, M.; Nabeshima, Y.; Takeuchi, T.; Kageyama, H.; Imaizumi, J.; Shibuya, H.; Akimoto, J. Synthesis of High-Capacity Ti- and/or Fe-Substituted $LiMnO_3$ Positive Electrode Materials with High Initial Cycle Efficiency by Application of the Carbothermal Reduction Method. *J. Power Sources* **2013**, *221*, 427−434.
(18) Kikkawa, J.; Akita, T.; Tabuchi, M.; Tatsumi, K.; Kohyama, M. Participation of Oxygen in Charge/Discharge Reactions in $Li_{1.2}Mn_{0.4}Fe_{0.4}O_2$: Evidence of Removal/Reinsertion of Oxide Ions. *J. Electrochem. Soc.* **2011**, *158*, A760−A768.
(19) Karthikeyan, K.; Amaresh, S.; Lee, G. W.; Aravindan, V.; Kim, H.; Kang, K. S.; Kim, W. S.; Lee, Y. S. Electrochemical Performance of Cobalt Free, $Li_{1.2}(Mn_{0.32}Ni_{0.32}Fe_{0.16})O_2$ Cathodes for Lithium Batteries. *Electrochim. Acta* **2012**, *68*, 246−253.

22314

dx.doi.org/10.1021/am5062882 | *ACS Appl. Mater. Interfaces* 2014, 6, 22305−22315

(20) Li, J.; Wang, L.; Wang, L.; Luo, J.; Gao, J.; Li, J.; Wang, J.; He, X.; Tian, G.; Fan, S. Synthesis and Characterization of Li-$(Li_{0.23}Mn_{0.47}Fe_{0.2}Ni_{0.1})O_2$ Cathode Material for Li-Ion Batteries. *J. Power Sources* **2013**, *244*, 652−657.

(21) Liu, G.-B.; Liu, H.; Wang, Y.; Shi, Y.-F.; Zhang, Y. The Electrochemical Properties of Fe-and Ni-Cosubstituted Li_2MnO_3 via Combustion Method. *J. Solid State Electrochem.* **2013**, *17*, 2437−2444.

(22) Sun, Y.; Ouyang, C.; Wang, Z.; Huang, X.; Chen, L. Effect of Co Content on Rate Performance of $LiMn_{0.5−x}Co_{2x}Ni_{0.5−x}O_2$ Cathode Materials for Lithium-Ion Batteries. *J. Electrochem. Soc.* **2004**, *151*, A504−A508.

(23) Morales, J.; Peres-Vicente, C.; Tirado, J. L. Cation Distribution and Chemical Deintercalation of $Li_{1−x}Ni_{1+x}O_2$. *Mater. Res. Bull.* **1990**, *25*, 623−630.

(24) Ammundsen, B.; Paulsen, J. Novel Lithium-Ion Cathode Materials Based on Layered Manganese Oxides. *Adv. Mater.* **2001**, *13*, 943−956.

(25) Yamada, A.; Chung, S. C.; Hinokuma, K. Optimized $LiFePO_4$ for Lithium Battery Cathodes. *J. Electrochem. Soc.* **2001**, *148*, A224−A229.

(26) Zhang, X.; Jiang, W. J.; Mauger, A.; Qilu; Gendron, F.; Julien, C. M. Minimization of the Cation Mixing in $Li_{1+x}(NMC)_{1−x}O_2$ as Cathode Material. *J. Power Sources* **2010**, *195*, 1292−1301.

(27) Wu, S.-H.; Liu, H.-Y. Preparation of α-$LiFeO_2$-Based Cathode Materials by an Ionic Exchange Method. *J. Power Sources* **2007**, *174*, 789−794.

(28) Johnson, C. S.; Kim, J.-S.; Lefief, C.; Li, N.; Vaughey, J. T.; Thackeray, M. M. The Significance of the Li_2MnO_3 Component In 'Composite' $xLi_2MnO_3\cdot(1−x)LiMn_{0.5}Ni_{0.5}O_2$ Electrodes. *Electrochem. Commun.* **2004**, *6*, 1085−1091.

(29) Lu, Z.; Dahn, J. R. Understanding the Anomalous Capacity of $Li/Li[Ni_xLi_{(1/3−2x/3)}Mn_{(2/3−x/3)}]O_2$ Cells Using In situ X-Ray Diffraction and Electrochemical Studies. *J. Electrochem. Soc.* **2002**, *149*, A815−A822.

(30) Li, J.; Li, J.; Luo, J.; Wang, L.; He, X. Recent Advances in the $LiFeO_2$-Based Materials for Li-Ion Batteries. *Int. J. Electrochem. Sci.* **2011**, *6*, 1550−1561.

(31) Morales, J.; Santos-Peña, J.; Trócoli, R.; Franger, S.; Rodríguez-Castellón, E. Insights into the Electrochemical Activity of Nanosized α-$LiFeO_2$. *Electrochim. Acta* **2008**, *53*, 6366−6371.

(32) Johnson, C. S.; Li, N.; Lefief, C.; Vaughey, J. T.; Thackeray, M. M. Synthesis, Characterization and Electrochemistry of Lithium Battery Electrodes: $xLi_2MnO_3\cdot(1−x)LiMn_{0.333}Ni_{0.333}Co_{0.333}O_2$ ($0\leq x \leq 0.7$). *Chem. Mater.* **2008**, *20*, 6095−6106.